European Rotorcraft Forum

A Theoretical Basis for Adverse Aircraft-Pilot Coupling

Edward Bachelder, edward.bachelder@sjsu.edu, San Jose State University Research Foundation, NASA Ames Research Center, Moffett Field, CA, USA.

Bimal Aponso, Bimal.L.Aponso@faa.gov, Chief Scientific & Technical Advisor for Dynamic Systems, Federal Aviation Administration, Seattle, WA, USA.

Abstract

Currently there is no reliable quantitative method for definitively predicting the likelihood for encountering Adverse Pilot Coupling (APC) during human-in-loop operation. This work examines APC characterized by oscillations near the: 1) rigid body dynamic mode frequency, and 2) closed loop neuromuscular (NM) mode frequency. The influence of pilot control input noise (pilot response that is not linearly correlated with the forcing function) on APC was also examined. The source of data for the work was a human-in-the-loop simulation experiment using an active sidestick where the independent variables were stick force gradient, stick sensitivity, and roll lag frequency. A specific combination of the experimental variables was observed to significantly influence the occurrence and repeatability of APC. The study developed a novel method to predict the propensity for APC that incorporates pilot noise estimation as part of pilot parameter estimation. Departing from the traditional method of using a high-frequency sum-of-sines forcing function to identify a pilot's NM frequency response, a less intrusive approach leveraging internal noise as the NM forcing function is employed instead. Preliminary results indicate that pilot internal noise originates primarily from the pilot visual equalization element. An adaptive pilot model incorporating a simple objective function and the observed relationship between noise and visual equalization and is shown to produce behavior that closely matches the experimental data. Based on APC occurrence observed in the study a new metric, Relative Margin Proximity (RMP), is proposed for assessing APC propensity. The adaptive pilot model was used to investigate vehicle configurations from an experimental data base that had been rated for APC severity. The RMP values produced by the pilot model for these configurations were consistent with their APC ratings.

1. AIRCRAFT PILOT COUPLING

Almost every aircraft since the inception of flying has experienced some form of Adverse Aircraft Pilot Coupling (APC), usually in early development phases and off-nominal flight conditions. A large body of research on the subject shows that fundamental APC is a closed-loop instability in the pilot-vehicle system when phase-margin is lost due, for example, to rapid changes in required pilot compensation due to task demands, increased lags in the flight control system due to failures or limits, etc. The advent of powered controls, artificial feel-systems, side-sticks and fly-by-wire control systems improved the performance and capabilities of aircraft but also introduced increased potential for APC by adding complexity to the flight control system in the form of artificial feel-systems, added time delay, structural modes and filters, and cockpit anthropomorphic effects with modern inceptor designs. This increase in flight control complexity also broadened the characteristics of APC as well the factors that trigger them (Refs. 1, 2).

The National Research Council published the results of a comprehensive study on APC in 1997 (Ref. 3). The study assessed APC-related aspects of past incidents and accidents, aircraft development processes, the introduction of FBW, and national and international efforts devoted to APC research. Reference 3 delineated the observed APC into three categories. Category I are those APCs that are linear in nature and result from excessive lag in the system that provides limited margin for the pilot to increase gain (usually to meet task performance demands) without decreasing closed-loop pilot-vehicle response damping resulting in response overshoots/bobbles and rarely, divergent oscillations. Categories II and III APC result when the response of the aircraft suddenly changes due to nonlinearities in the system that are triggered by pilot input. In Category II APCs, the source of these nonlinearities is control surface rate or position limiting. In Category III, the sources of the nonlinearities are more complex such as structural and aeroelastic effects. The pilot's arm-neuromuscular system has historically been included in this category (Ref. 3), but it will be demonstrated that despite its complexity the neuromuscular system appears to behave in a linear fashion when contributing to APC.

ADS-33 (Ref.4) has an established set of quantitative aircraft response design criteria related to handling qualities (HQ) level for various rotorcraft Mission Task Elements (MTEs). These criteria may be used throughout the rotorcraft design cycle and verified through flight test system identification and MTE demonstration maneuvers. A key requirement in ADS-33 is the bandwidth and phase delay criterion that is based on the open-loop frequency response of the aircraft. This criterion captures the phase loss characteristics in the frequency region of closed-loop pilot control and is indicative of the pilot compensation required for good task performance. Since the precise frequency at which a pilot would operate and the actual

Presented at the 48th European Rotorcraft Forum, Switzerland, 6-8th September 2022.

compensation employed is unknown and currently cannot be established, there is inherent uncertainty factored into the specifications and the projected influence of a particular design. At present there is no reliable quantitative method for assessing APC during human-in-loop (HIL) operation.

A particular form of APC is a ratchet phenomenon that was noticed in high-performance fighter aircraft usually with isotonic sticks and in the roll axis. This "roll-ratchet" was prevalent in the USAF F-16 aircraft that used an isotonic side-stick. A series of in-flight and ground-based flight simulation studies investigated lateral handling qualities with side-sticks (Ref. 5) and identified several instances of APC and roll-ratchet. The work in Ref. 6 examined the roll-ratchet phenomenon and identified the pilot arm-neuromuscular dynamics as the most probable causal factor using an analytical approach that included previously identified pilot arm-neuromuscular dynamics (Refs. 7, 8) in the pilot-vehicle loop with high-performance aircraft roll dynamics. This hypothesis was based primarily on the proximity of the ratchet frequency to the neuromuscular (NM) mode frequency and the large frequency separation between the ratchet frequency (usually 2-3 Hz) and the identified crossover frequency (approximately 0.5-1.0 Hz). A follow-on ground-based simulation study in Ref. 9 solidified these findings and provided evidence that inceptor force-feel gradient was a likely factor with stiffer force-feel gradients being more likely to cause roll-ratchet.

The formative analysis in Refs. 6 and 9 modeled the NM system as static in the open-loop pilot-vehicle sense. Although the existence of the NM mode was observed in ground-based and in-flight simulation studies, there was no clear indication of an instability at that frequency when the open loop pilot-vehicle describing functions were examined as the phase criterion indicated stability. Subsequent analysis by Hess (Ref. 10) and Mulder (Ref. 11) indicated that the pilot arm-NM dynamics were potentially adaptable and an integral component of the pilot compensation necessary for the task. This work herein presents data suggesting that the NM system is even more flexible than the adaptivity proposed by Hess' Structural Model (Ref. 10).

2. NEUROMUSCULAR RESPONSE

The history of neuromuscular (NM) model development is summarized in Ref. 12. The closed-loop NM system has typically been modelled in manual control as having one lightly damped mode associated with the controlling limb's mass, damping and stiffness (Ref. 13). In Ref. 14 Gordon-Smith investigated the effects of manipulator dynamics on human operator response, and Figure 1 shows the frequency response data computed in this study for a free moving inceptor. Beyond approximately 10 rad/s the magnitude variability rapidly increases to where the standard deviation is larger than the mean. This likely is due to the extreme difficulty associated with an operator being able to track signals (even a single sine wave) above 10 rad/s.

For single sine wave tracking McRuer (Ref. 15) states "From about 2 Hz (12.5 rad/s) to the neuromuscular response limit of 5 to 10 Hz, the operator only uses an internal pattern generator loop to roughly approximate the displayed amplitude and frequency, usually undershooting both." Thus, it can be inferred that attempting to probe the NM system above 10 rad/s employing sum-of-sines (SOS) tracking likely introduces artifacts that significantly compromise measurement of what is being analyzed. Furthermore, real-life tracking during operational manual tracking tasks almost never encounters a disturbance that contains appreciable power at frequencies greater than 10 rad/s. An alternative method for probing the NM system that exerts minimal influence on what is being observed would appear to be desirable.

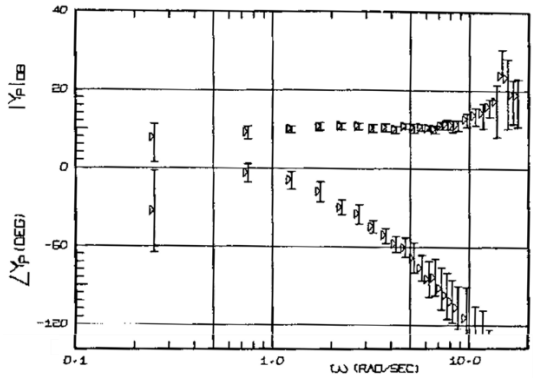

Figure 1. Pilot describing function variability across subjects for free-moving manipulator (Ref.14)

In Ref. 15 McRuer characterized operator noise as 'observation' noise. This same noise might be expected to excite the NM system in a repeatable manner without the need for an external forcing function that is generating power in the vicinity of NM modes. Such excitation was observed not only with the stick PSDs of the current experiment, but also with previous experiments the author has conducted (Refs. 12, 16).

3. NEUROMUSCULAR SYSTEM MODELING

In Ref. 17 Bachelder modeled the neuromuscular (NM) system when force feedback is available as shown in Figure 2. The open-loop NM system G_{NM}^{OL} is represented as a second order system with a pure time delay

$$G_{NM}^{OL} = \frac{{\omega_{NM}^{OL}}^2 e^{-\tau_{NM}s}}{(s^2 + 2\zeta_{NM}^{OL}\omega_{NM}^{OL} + {\omega_{NM}^{OL}}^2)} \quad (1)$$

and the proprioceptive sensing and feedback element G_{PF} is modeled as a first-order lead-lag with a proportional gain K_{PF}.

Presented at the 48th European Rotorcraft Forum, Switzerland, 6-8th September 2022.

$$G_{PF} = K_{PF}\frac{\omega_{Lg}(s+\omega_{Ld})}{\omega_{Ld}(s+\omega_{Lg})} \quad (2)$$

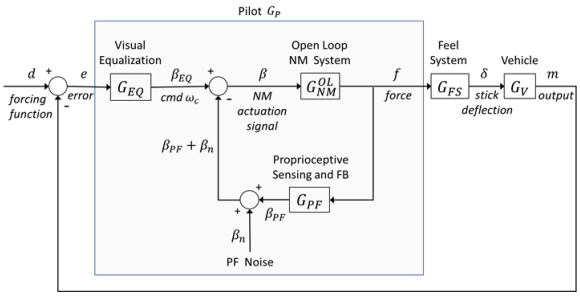

Figure 2. Pilot neuromuscular model.

G_{NM}^{OL} has typically been modelled in manual control as having one mode ω_{NM}^{OL} fixed at approximately 10 rad/s with a damping ratio ζ_{NM}^{OL} of 0.7 (Hess' Structural Model, Ref. 10). The closed-loop natural frequency ω_{NM}^{CL} has been observed to range from 5 rad/s (Ref. 18) to approximately 20 rad/s (Ref. 19).

The Structural Model assumes stick deflection is the NM feedback signal, and that the feel system is included in the NM control loop. This provides the degree of freedom to shift ω_{NM}^{CL} below the open loop NM frequency (ω_{NM}^{OL}) which the Structural Model assumed fixed at 10 rad/s. However, in Ref. 20 Bachelder presented evidence that force (not stick deflection) is predominantly employed for control feedback when the inceptor is spring centering. Without the feel system in the loop, NM feedback will produce a ω_{NM}^{CL} that is greater than or at least equal to ω_{NM}^{OL}, i.e., when ω_{NM}^{CL} has been observed to be less than 10 rad/s ω_{NM}^{OL} must likewise be less than 10 rad/s.

Also shown in Figure 2 is NM noise *n* arising from proprioceptive sensing and feedback signal generation. The NM feedback signal $\beta_{\dot{m}}$ is effectively inner-loop rate feedback, to which noise is added. $\beta_{\dot{m}}$ serves to condition the output m such that its rate $\dot{m}$ is proportional to the error signal e (i.e., the system conforms to the Crossover Model).

The visual equalization element G_{EQ} is represented as a gain K_{EQ} and pure time delay τ_{EQ}. This delay is associated with visual and central nervous system processing

$$G_{;EQ} = K_{EQ}e^{-\tau_{EQ}s} \quad (3)$$

The output of G_{EQ} (β_{EQ}) is the command signal for the crossover frequencyω_c. The force produced by the operator is exerted on the feel system G_{FS} yielding stick deflection, which is received by the vehicle G_V transfer function and generates the vehicle output *m*.

4. ROLL RATCHET

In Ref. 21, Bachelder employed wavelets to identify pilot parameters from flight test data of a lateral handling qualities study conducted with the USAF variable stability NT-33A (Ref. 22). The study investigated lateral handling qualities issues including stick feel system dynamics, gradient, and sensing type (i.e., position or force) in combination with roll mode time constant variations. The results indicated that: a lightly-damped mode in the open-loop system is introduced by the human pilot at frequencies higher than the task bandwidth; and a direct correspondence exists between the peak amplitude of the lightly-damped mode and the occurrence of roll ratchet. Four sum-of-sines roll tracking tasks were examined and shown in Table 1. All four runs were flown by the same pilot with the same roll control sensitivity (18 deg/sec/lb). As identified in Table 1 the first selected case (Run 4069.1) featured a slow feel system (13 rad/sec) and the highest roll mode time constant. This configuration received a Level 1 handling qualities rating for the tracking task evaluation with no roll ratchet or PIO tendencies. The remaining three configurations listed in Table 1 had significant handling qualities deficiencies. The Run 4069.4 configuration had a degraded feel system combined with the highest roll damping and resulted in continuous roll ratchet and a Level 3 handling qualities assessment (see Figure 3). Run 4161.3 had the fast feel system, a 55 msec command path time delay, and medium roll damping. This run exhibited intermittent roll ratchet and a Level 3 handling qualities rating. Run 4176.1 was configured as 4161.3 except with no command path time delay, yielding Level 3 handling qualities with continuous lower frequency ratchet.

Table 1. System Characteristics and Flight Results.

	Command Path Dynamics		Roll Mode	Flight Results	
Run No.	ω_{FS} (rad/sec)	τ (msec)	T_r (sec)	Description	HQR
4069.1	13	None	0.40	No sustained ratchet	2
4069.4	8	None	0.15	Continuous ratchet	8
4161.3	26	55	0.25	Intermittent ratchet	7
4176.1	26	None	0.25	Lower frequency ratchet	7

The following comment is taken from Ref. 23 on how a minor change (in this case a decrease in control sensitivity) can produce substantial differences in HQs: *Without changing the feel-system dynamics, the roll mode time constant, or the mechanization of force-sensing commands, what was an overly abrupt HQR = 7 airplane is now almost perfect.*

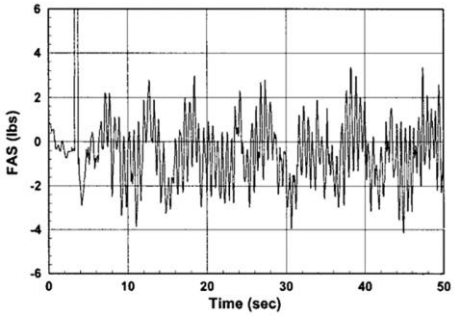

Figure 3. Time histories for flight 4069.4 showing stick force history (Ref. 21).

5. EXPERIMENT

A simulation experiment for examining pilot-vehicle oscillations was conducted using the Brunner active inceptor positioned for center-stick use (Figure 4).

Figure 4. Brunner active inceptor positioned for center-stick use.

The task was lateral compensatory tracking using the compensatory visual display shown in Figure 5, and the objective was to align ownship's symbol with the stationary target. Ownship motion was driven by a sum-of-sines (SOS) forcing function containing eleven non-harmonic sine waves, where the amplitudes decreased logarithmically (power of 10) with increasing frequency. SOS frequency ranged from 0.048 to 4.65 rad/s.

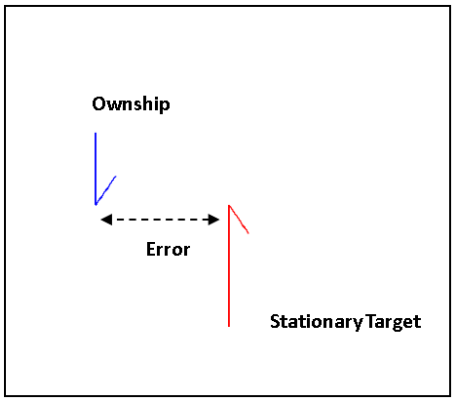

Figure 5. Compensatory tracking display used in force-feedback experiment.

The transfer function G_V governing ownship motion was

$$G_V = K_V \frac{1}{s(s+p)} \quad (4)$$

where p is the roll lag frequency. The independent variables were stick force gradient (K_{FG}), stick gain (K_V), and roll lag frequency (p), shown in Figure 6. Each configuration was flown three times, and run duration was 60 seconds. Bedford workload ratings were collected following the completion of each configuration's set of three runs. Time histories of 108 runs for the 36 configurations were recorded. The experiment used a single subject with 1,000 hours of military flight time.

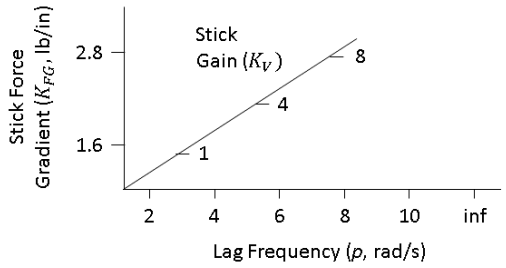

Figure 6. Experimental independent variables.

Stick Dynamics

The cyclic inceptor dynamics are defined by its mass, damping coefficient, and spring force gradient, from which the natural frequency and damping ratio can be computed. The inceptor displacement δ due to force input f can be modeled as a second order system:

$$\frac{\delta}{f} = \frac{\omega_n^2/K_{FG}}{s^2+2\zeta\omega_n s+\omega_n^2} \quad (5)$$

where the K_{FG} is the force gradient, ω_n is the natural frequency, and ζ is the damping ratio. Force was measured for various static stick deflections to compute the force gradient. Using Eqn. **5** ω_n and ζ were estimated from the measured stick deflection and force obtained from a manual frequency sweep. Figure 7 compares the normalized actual stick deflection (denoted by black) with the simulated deflection (denoted by magenta) using ω_n and ζ that were estimated . Table 2shows the inceptor characteristics, where mass m and damping coefficient b were computed using the relations $m = {\omega_n}^2/k$ and $b = 2m\zeta\omega_n$.

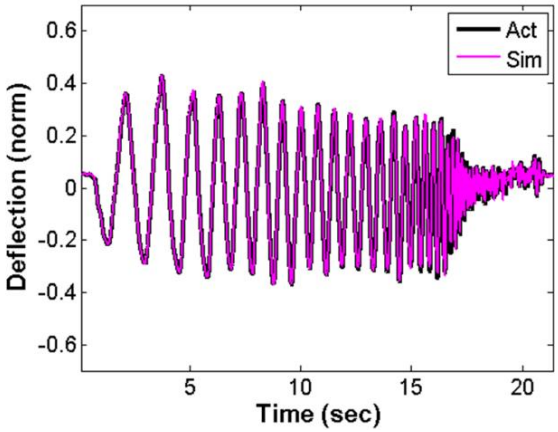

Figure 7. Inceptor dynamics identification: comparison of actual to simulated stick response to measured force.

Table 2. Identified inceptor characteristics.

Natural Frequency ω_n (rad/s)	Damping Ratio ζ	Force Gradient k (lb/in)	Damping Coefficient b (lb/in/s)	Mass m (lb)
34.4	0.08	2.87	0.01	0.03

The inceptor mass, spring gradient and damping were such that the second order mode at ω_n effectively lies beyond the frequency regions associated with feedback control and NM modal response (Figure 8).

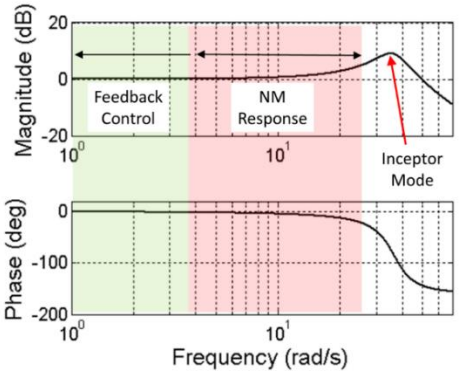

Figure 8. Frequency response of inceptor (longitudinal axis) relative to regions of feedback control and NM response.

6. PILOT PARAMETER ESTIMATION USING INTERNAL NOISE

Figure 9 shows stick deflection power spectral density (PSD) computed from a run. Two lightly damped modes are observed located roughly at 9 rad/s and 25 rad/s. The origin of these two modes must be related to noise since their frequencies lie above the highest SOS frequency (5 rad/s) and below the inceptor's resonant mode (35 rad/s). Reference 17 hypothesized that the lower frequency mode corresponds to the forearm motion, and the higher mode with wrist/finger motion.

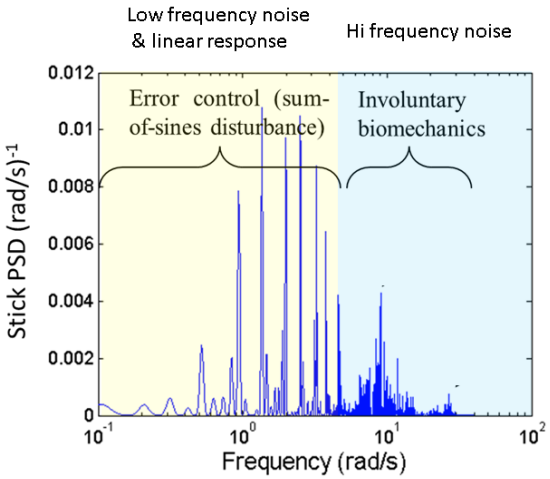

Figure 9. Stick spectral content from an experimental run showing regions of error control and involuntary biomechanics.

Referring to the model in Figure 2 it can be shown that the stick deflection δ is related to the internal noise signal β_n by

$$\delta = G_{d\delta}\left(d - \beta_n G_{EQ}^{-1}\right) = \delta_{lin} + \delta_n \qquad (6)$$

where δ_{lin} and δ_n are the linear and noise responses of the stick, and $G_{d\delta}$ is the closed-loop stick transfer function. Using iteration across a range of values for each parameter, estimation of the pilots parameters is conducted by minimizing a cost function J (Eqn. 7). J is the product of two frequency-domain components (one low the other high frequency corresponding to the error control and involuntary regions shown in Figure 9), and a low frequency time domain component:

$$\begin{aligned} J &= \prod J_i, \\ J_1 &= \left\{\sum_j \left|\sum_i S_{\delta\delta_{sim,i,j}} - \sum_i S_{\delta\delta_{i,j}}\right|\right\} \\ J_2 &= \left\{\sum_q \left|S_{\delta\delta_{sim,q}} - S_{\delta\delta_{filt,q}}\right|\right\} \\ J_3 &= \left\{\sum_r \left|m_{sim,lo}(t_r) - m_{lo}(t_r)\right|\right\} \end{aligned} \qquad (7)$$

Referring to J_1, j spans the number of windows assigned to each discrete SOS frequency ω_j > 0.1 rad/s, and i spans the number of frequencies assigned to each window j. A window is centered on ω_j and extends 7% of the frequency to either side of it. The SOS frequencies are

$$\omega_j = {}^{2\pi}/_{131}*(3, 5, 11, 19, 29, 41, 53, 67, 79, 97)$$

Figure 10 shows the PSD of the actual and simulated stick in the frequency region operated on by J_1 (0.1<ω<5 rad/s). The simulated stick is computed using as $\delta_{sim} = dG_{d\delta}$.

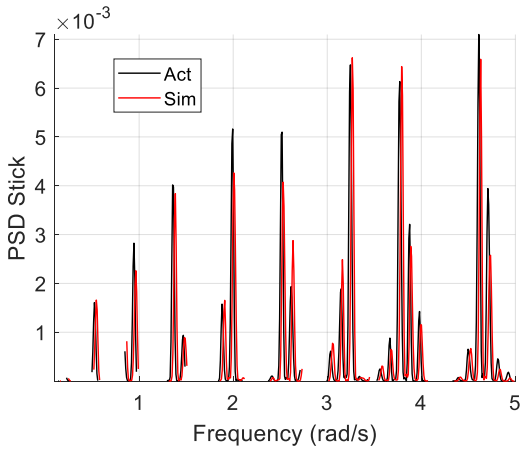

Figure 10. PSD of actual and simulated stick during model estimation (low frequency range).

Operating in the frequency range beyond the forcing function, J_2 compares the actual stick PSD with a simulated stick whose source, $\beta_{n,hi,sim}$, is uncorrelated noise. Assuming this to be driven by unity power white noise n_w scaled by the factor N,

$$\beta_{n,hi,sim} = N n_w \qquad (8)$$

Using Eqn. 6 the simulated high frequency stick is

$$\delta_{n,hi,sim} = \beta_{n,hi,sim}\, G_{EQ}^{-1}\, G_{d\delta} = N n_w\, G_{EQ}^{-1}\, G_{d\delta} \qquad (9)$$

which is a function of the estimated pilot's parameters contained in $G_{d\delta}$ and G_{EQ}. In Figure 11 the actual high frequency stick power is filtered across frequency (Ref. 24), denoted by the black line. The ratio of the sum of this filtered power to the sum of the simulated stick power is equal to the square of the power of $\beta_{n,hi,sim}$,

$$N^2 = \sum S_{\delta\delta_{filt,}} / \sum S_{\delta\delta_{sim}} \quad (10)$$

From Eqn. 9 the simulated stick power is computed and J_2 compares this with the actual filtered stick power at each frequency ω_q spanning 5 to 15 rad/s.

For brevity the low pass filter operation conducted at 5 rad/s on δ is denoted as LPF5(δ), and the high pass filter operation conducted at 5 rad/s on δ as HPF5(δ).

J_3 compares the low frequency simulated vehicle output LPF5(m_{sim}) with the actual low frequency vehicle output LPF5($m = dG_{dm}$) at each time step t_r shown in Figure 12. Although m is already constrained to low frequency due to the forcing function d, it is low-pass filtered to be in phase with LPF5(m_{sim}). The minimized cost function J in Eqn. 7 establishes the estimated pilot parameter set associated with the run's data.

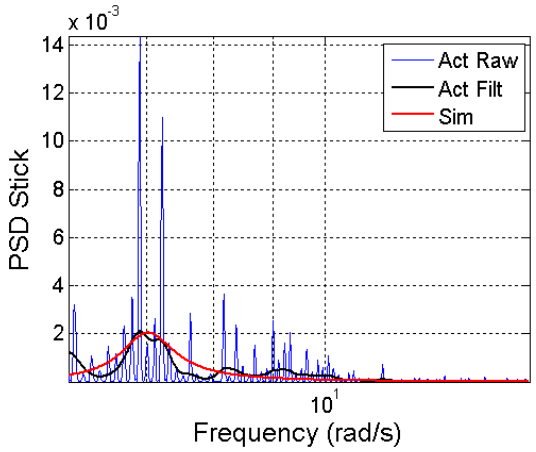

Figure 11. PSD of actual and simulated stick during model estimation (high frequency range).

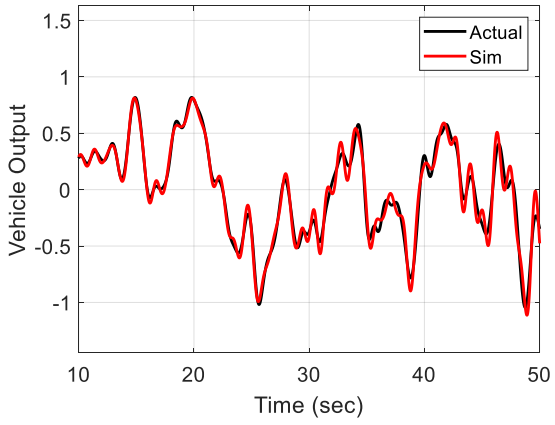

Figure 12. Low frequency time response of actual and simulated stick during model estimation.

Relative Stick Noise Content

The noise content in the pilot's stick signal is now examined. The linear stick response δ_{lin} to the forcing function d is

$$\delta_{lin} = G_{d\delta} d \quad (11)$$

The low frequency stick noise is computed by subtracting LPF5(δ_{lin}) from LPF5(δ) (the high frequency stick noise is simply HPF5(δ)),

$$\delta_{n,lo} = \delta_{lo} - \delta_{lin,lo} \quad (12)$$

Figure 13 compares the actual low frequency stick ($\delta_{lo} = \delta_{lin,lo} + \delta_{n,lo}$) to its low frequency noise for the worst performing condition ($K_{FG} = 2.8$ rad/s, $p = 2$ rad/s, $K_V = 1$, see Figure 21 in the *Results* section). The ratio of noise to total signal is 92%. In Figure 14 the best performing condition ($K_{FG} = 2.8$ rad/s, p = infinity, $K_V = 8$) yields a noise-to-signal ratio of 33%.

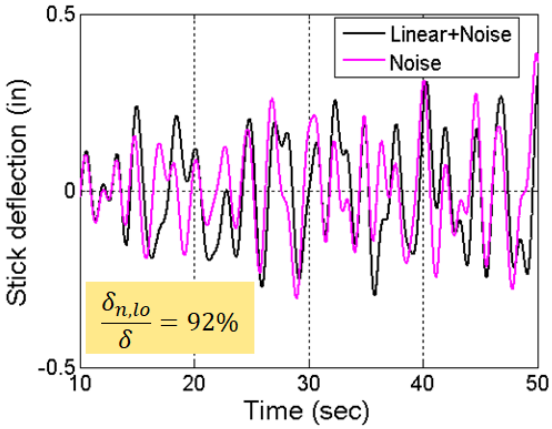

Figure 13. Low frequency stick response (actual stick, $K_V = 1, p = 2\frac{\text{rad}}{\text{s}}, K_{FG} = 2.8$ lb/in).

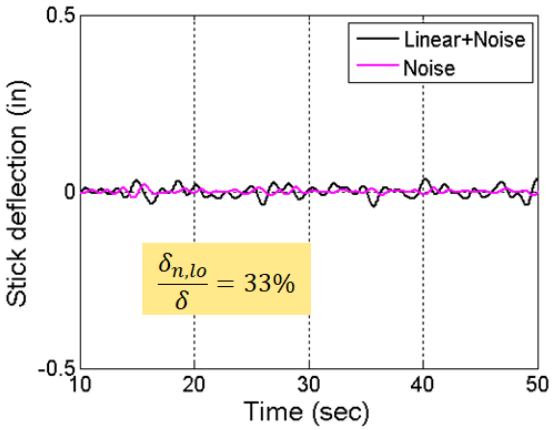

Figure 14. Low frequency stick response (actual stick, $K_V = 8, p = \text{inf}, K_{FG} = 2.8$ lb/in).

In Figure 15 and Figure 16 the high frequency noise to total stick ratios for the worst and best performing conditions are 37% and 62%, respectively.

Drivers of Internal Noise

The correlation between internal noise and pilot parameters was investigated to assign potential causality. From Eqn. 6 internal noise can be written as

$$\beta_n = G_{EQ}\left(d - \delta G_{d\delta}^{-1}\right) \quad (13)$$

The power of the low and high frequency regions of β_n is computed by summing PSD as follows:

$$\sigma^2_{\beta_{n,lo}} = \frac{1}{2\pi}\sum_{\omega=.1}^{\omega=5} S_{\beta\beta_n \Delta\omega}$$

$$\sigma^2_{\beta_{n,hi}} = \frac{1}{2\pi}\sum_{\omega=.5}^{\omega=15} S_{\beta\beta_n \Delta\omega} \quad (14)$$

The combination of variables correlating highest with $\beta_{n,lo}$ was the ratio of equalization gain to crossover frequency, K_{EQ}/ω_c, seen in Figure 17 (97% correlation). Here the noise to stimulus ratio is approximately 1:5. Thus, low frequency noise is directly proportional to the pilot's equalization gain and inversely proportional to crossover. The highest correlation with $\beta_{n,hi}$ was obtained using $\beta_{n,lo}$ (90%), shown in Figure 18. Here the noise to stimulus ratio is approximately 1:2. Correlation was computed using 95% of the data. All other pilot parameters and their combinations correlated poorly with the noise; thus, it appears that most of the noise is associated with the equalization element G_{EQ}. Reference 25 ascribes this element to retinal and central equalization associated with the visual channel.

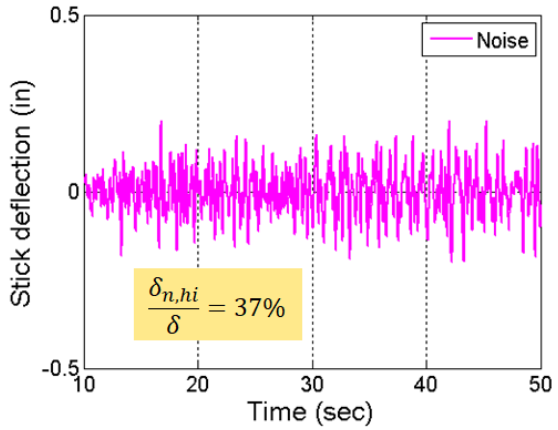

Figure 15. High frequency stick response (actual stick, $K_V = 1, p = 2\frac{\text{rad}}{\text{s}}, K_{FG} = 2.8$ lb/in).

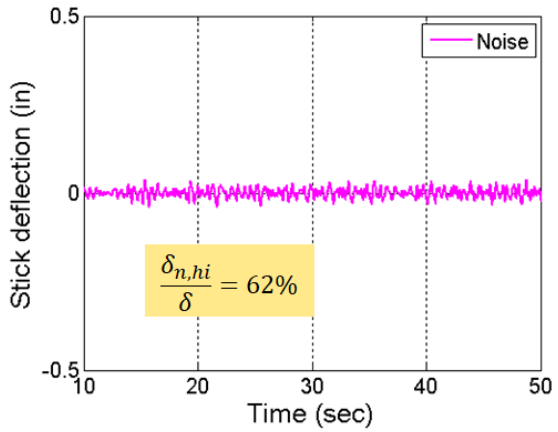

Figure 16. High frequency stick response (actual stick, $K_V = 8, p = \text{inf}, K_{FG} = 2.8$ lb/in).

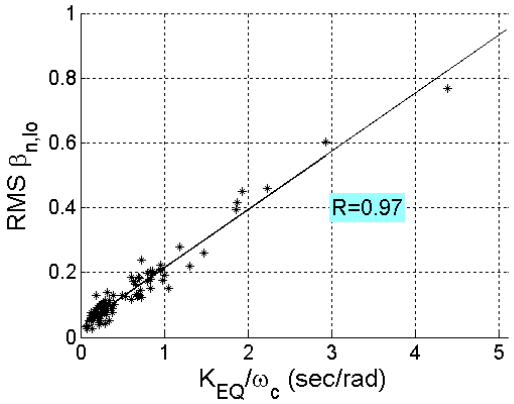

Figure 17. Low frequency noise $\beta_{n,lo}$ vs equalization gain/crossover ratio.

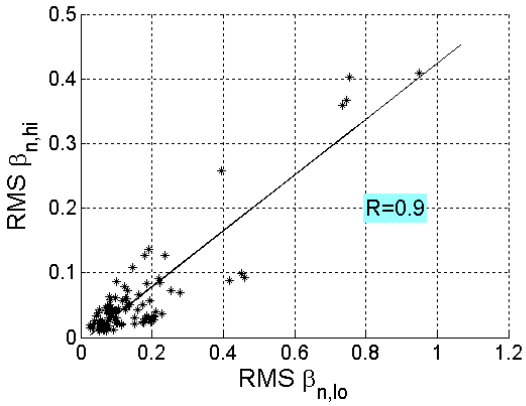

Figure 18. High frequency noise $\beta_{n,hi}$ vs $\beta_{n,lo}$.

7. EXPERIMENTAL RESULTS

Investigating metrics of APC likelihood

In Figure 19 gain and phase margin are depicted, the first associated with open loop (G_{em}) phase crossover, $\omega_{c\phi}$, and the second with gain crossover (ω_c). The pilot's dynamics will influence to some extent the location of the closed loop rigid body mode ω_{RB}, and to a great extent the location of the closed loop mode associated with the pilot's NM mode (not shown in the figure to maximize view of the stability margins). It will be shown that the distance between the two crossover frequencies relative to the phase crossover, coined Relative Margin Proximity (RMP), appears to be a key metric associated with APC.

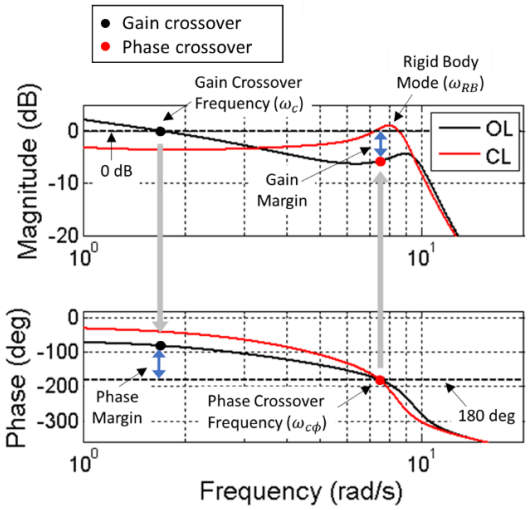

Figure 19. Stability margin definitions.

Tracking error (normalized by the standard deviation of the forcing function *d*) is shown in Figure 20 and Figure 21 for the low and high stick force gradients (K_{FG} = 1.6 and 2.8 lb/in, respectively). The higher force gradient produces significantly better tracking error than the low gradient using the highest stick sensitivity (K_V = 8). This is consistent with significantly higher crossover frequencies for K_{FG} = 2.8 comparing Figure 22 and Figure 23.

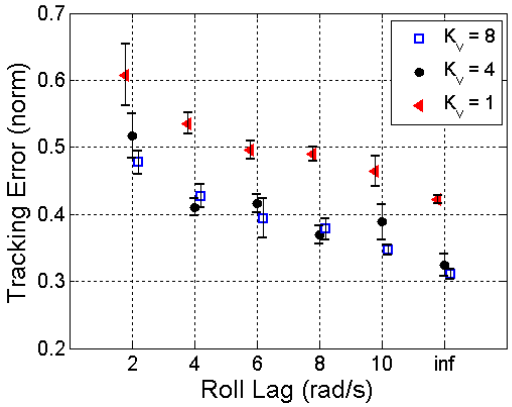

Figure 20. Tracking error (K_{FG} = 1.6 lb/in).

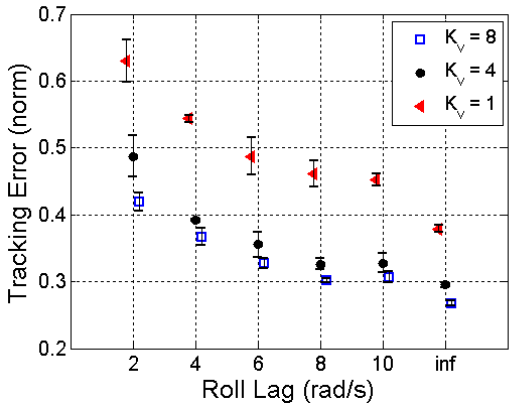

Figure 21. Tracking error (K_{FG} = 2.8 lb/in).

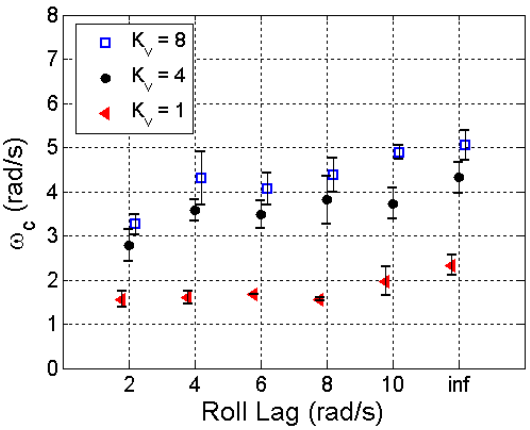

Figure 22. Crossover frequency (K_{FG} = 1.6 lb/in).

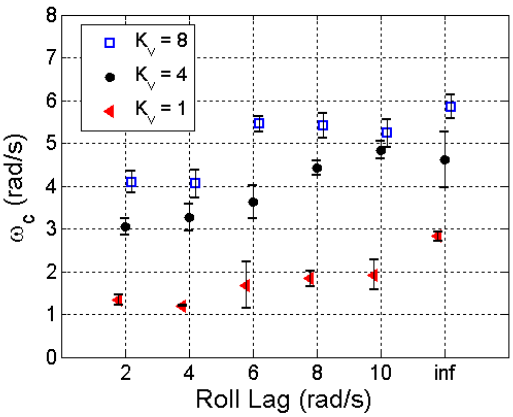

Figure 23. Crossover frequency (K_{FG} = 2.8 lb/in).

In Eqn. 15 ρ is defined as the ratio of high to low frequency stick power. In Figure 24 a roll lag of 4 rad/s using the low force gradient yields the highest ρ. In Figure 25 a roll lag of 6 rad/s produces the highest ρ using the higher force gradient. This condition's ρ value is significantly higher than all other conditions and is denoted by a red asterisk as the APC condition.

$$\rho = \sum_{\omega>5}^{\omega=15} S_{\delta\delta} / \sum_{\omega>1}^{\omega=5} S_{\delta\delta} \quad (15)$$

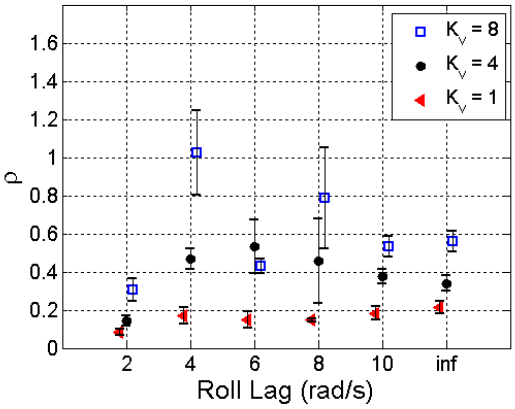

Figure 24. Ratio of high to low frequency stick power (K_{FG} = 1.6 lb/in).

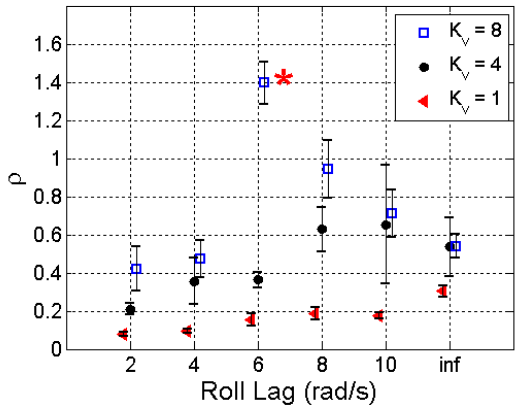

Figure 25. Ratio of high to low frequency stick power (K_{FG} = 2.8 lb/in), red asterisk denotes APC condition.

Figure 26 and Figure 27 show the frequency separation between phase crossover and the closed loop rigid body mode (to reduce visual clutter only the high stick gain conditions are given). Near-alignment is observed with the low force gradient at a roll lag of 4 rad/s, and for roll lags of 2, 4, and 6 rad/s for the high force gradient. This indicates that alignment is a necessary but not sufficient criterion for APC.

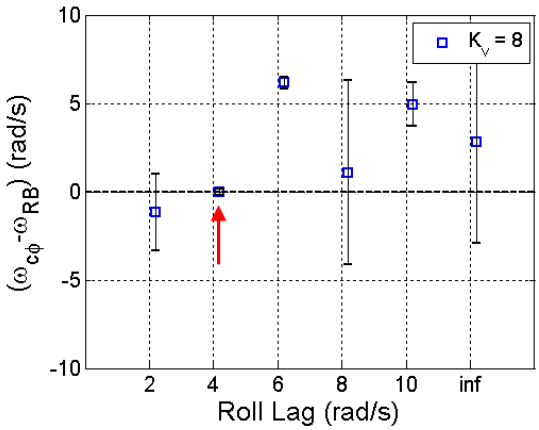

Figure 26. Proximity of rigid body mode to phase crossover (K_{FG} = 1.6 lb/in, K_V = 8), red arrow indicates near-alignment.

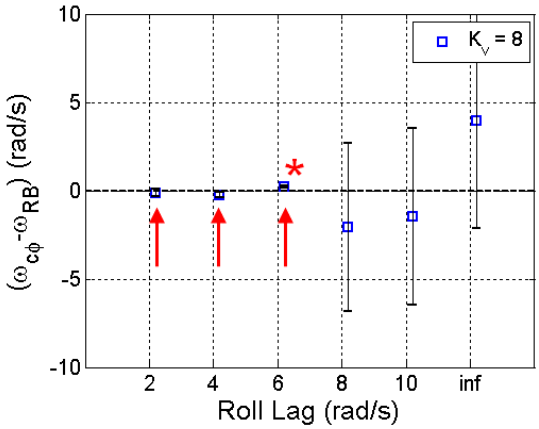

Figure 27. Proximity of rigid body mode to phase crossover (K_{FG} = 2.8 lb/in, K_V = 8), red arrows indicate near-alignment. red asterisk denotes APC condition.

Eqn. 16 defines the metric Relative Margin Proximity

$$RMP = \frac{(\omega_{c\phi} - \omega_c)}{\omega_{c\phi}} \text{ x } 100\% \qquad (16)$$

(RMP), and Figure 28 and Figure 29 present RMP for low and high force gradient. RMP for the high force gradient, high stick gain, and roll lag of 6 rad/s (the APC condition) is significantly lower than the other 35 conditions. In Figure 29 the RMP threshold separating the APC condition from the others is approximately 27%, and this is called the RMP cutoff and shown as a red line. Figure 30 plots high-to-low stick power ratio against RMP using the aggregate data. Using the 27% cutoff there is only one false positive out of the 105 non-APC runs.

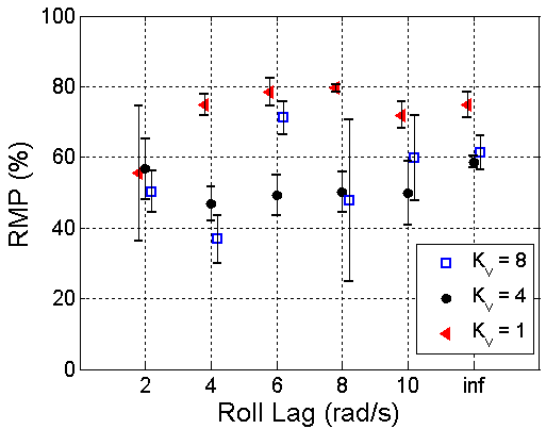

Figure 28. Relative Margin Proximity (K_{FG} = 1.6 lb/in).

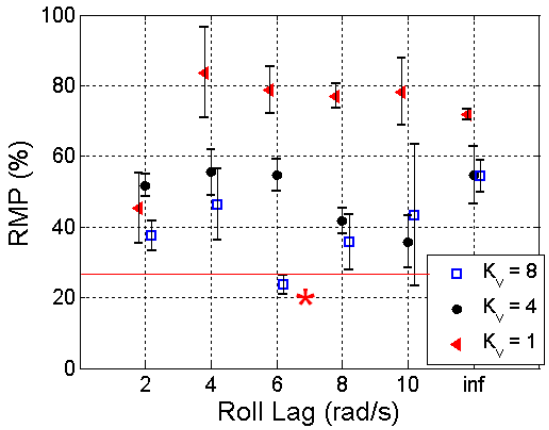

Figure 29. Relative Margin Proximity (K_{FG} = 2.8 lb/in), red asterisk denotes APC condition, red line marks 27% RMP cutoff.

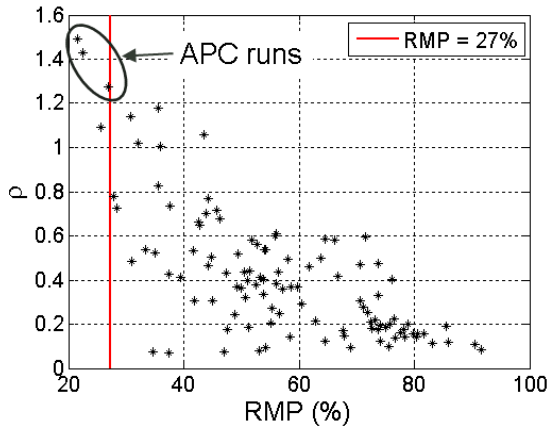

Figure 30. Ratio of high to low frequency stick power vs. Relative Margin Proximity showing 27% RMP cutoff.

Bedford workload ratings (Ref. 26) were collected after each configuration's three runs, thus there is no standard deviation bar. Figure 31 and Figure 32 give the workload ratings for the low and high force gradient conditions. In Figure 32 the high stick gain workload is relatively uniform except for the APC event, where it jumps by more than two. Higher frequency APC tends to be more of an annoyance (for short term operation) rather than a hindrance, corroborated by the good tracking performance for this condition seen in Figure 21. The pilot appears to accept the nuisance of ratchet since the pilot compensation that produces it also offers the best performance.

8. APC PREDICTION USING PILOT MODEL

The relationships identified earlier between pilot internal noise, equalization gain, and crossover were implemented in the pilot model to generate stick noise that adapted to pilot behavior. A pilot cost function given by Eqn. 17 was developed that employs tracking error and peak magnitude of the open loop NM response (Figure 33),

$$J = {\sigma_e}^2 \left|G_{OL,NM}\right|^{0.5} \qquad (17)$$

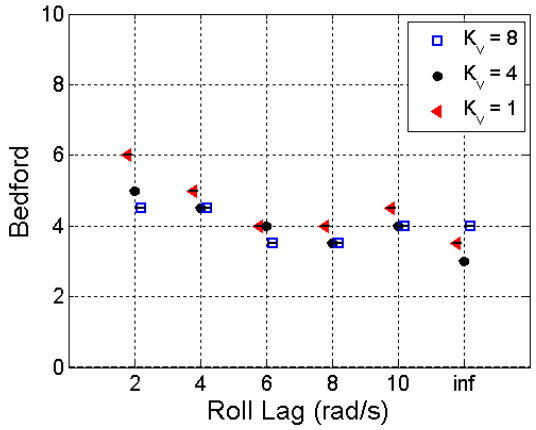

Figure 31. Bedford ratings (K_{FG} = 1.6 lb/in).

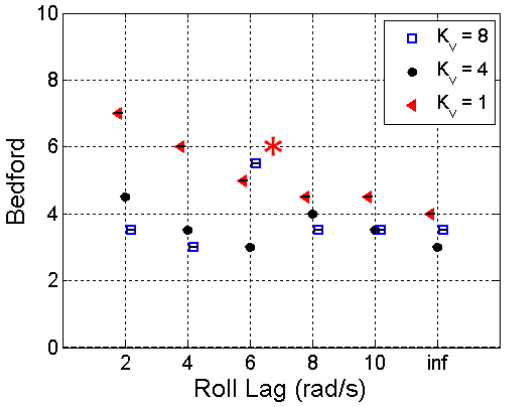

Figure 32. Bedford ratings (K_{FG} = 2.8 lb/in, red asterisk denotes APC condition).

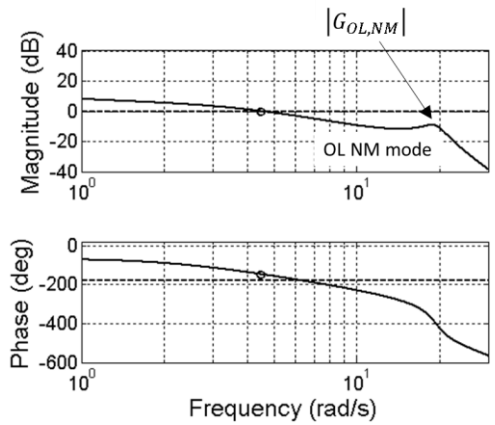

Figure 33. Open loop frequency response showing peak magnitude of NM mode.

The pilot parameters that minimize this cost function produced time and frequency response that closely matched the experimental data for both APC and non-APC runs. Figure 34a shows the frequency response corresponding to the estimated pilot parameters of an APC run, and below it is the actual stick time response exhibiting a pronounced, sustained oscillation at 7.2 rad/s. The frequency and stick time response produced by the pilot model compare quite well in Figure 35, both visually and in terms of RMP and oscillation frequency.

APC Simulation Case Studies

Reference 27 provides experimental flight test data base for examining severe, fully-developed APCs. These experiments used the USAF/Calspan variable stability NT-33 aircraft, with three test pilot subjects, in landing approach tasks. Each pilot flew three approaches to a desired touchdown point: one straight in; the other two with left and right-side lateral offsets followed by a correction to centerline.

In Table 3 the three - 1 entries are the baseline configurations; the remaining entries are the effective vehicle dynamics that produced severe APC which comprise the baseline dynamics plus the additional lags

listed. The configurations 3-1 and 3-13 (good and poor ratings) are examined here.

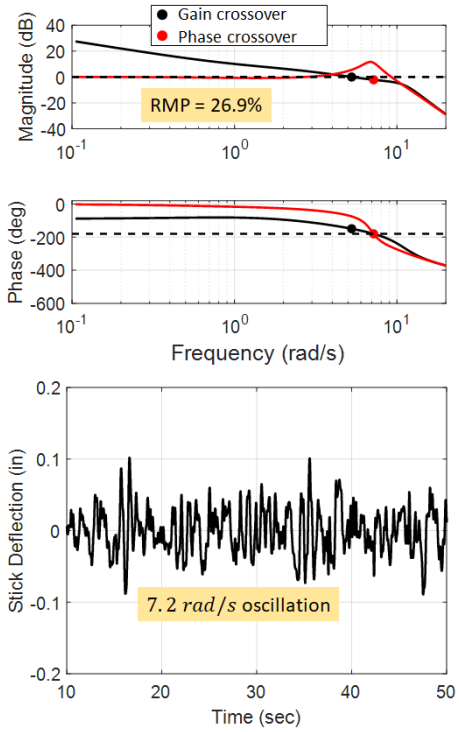

Figure 34. a) Estimated actual open and closed loop frequency response (APC run); b) Stick response.

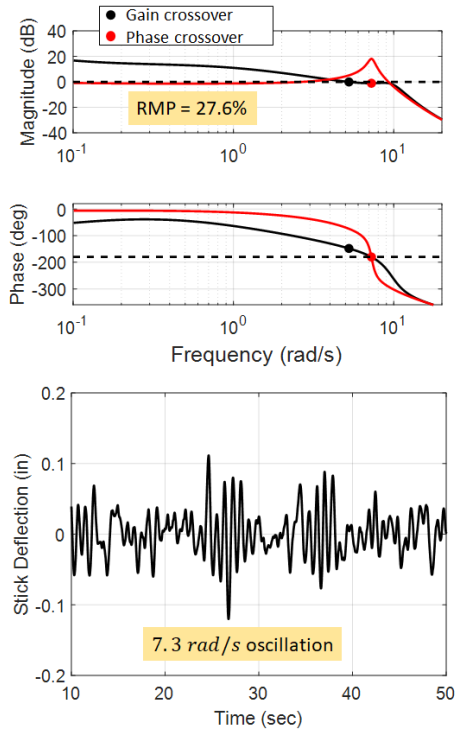

Figure 35. a) Modeled open and closed loop frequency response (APC run, all parameters free); b) Stick response.

Using the pilot model, crossover frequency was incremented representing increased requirement for precision tracking. The poor vehicle configuration 3-13 is examined first. Crossover is set to 1 rad/s in Figure 36, and the model generates pilot parameters that yield an RMP of 67%, well above the 27% cutoff. In Figure 37 crossover is 2.2 rad/s, RMP drops to 30%, and there is a pronounced 3 rad/s stick oscillation associated with the rigid body mode (ω_{RB}). Note that although crossover has more than doubled in value, neither ω_{RB} nor $\omega_{c\phi}$ has shifted. In Figure 38 crossover is increased to 2.4 rad/s, and we see that a 16.2 rad/s oscillation is now superimposed on the 3 rad/s motion associated with the rising peak of the NM mode. RMP is at 20% - below the 27%% cutoff – and when crossover is barely incremented to 2.45 rad/s in Figure 39 instability results.

Table 3. Bjorkman's PIO configurations (Ref.).

Configuration	Transfer Function	Ratings CH	Ratings PIOR	Attitude Bandwidth ω_{BW}	Phase Delay τ_p	Average Phase Rate deg/rad/sec	Average Phase Rate deg/Hz	
2-1	$\frac{2.46E7(.0845)(.699)}{[.15,.17][.63,2.4][.6,26][.7,75]}$	2/2/3	1/1/1	3.03	0.055	6.27	39.38	
2-5	$\frac{1.98E7(.0845)(.699)}{[.15,.17][.63,2.4][.6,26][.7,75]}\frac{1}{(1)}$	10/7/10	4/4/5	1.38	0.235	26.91	169.08	
2-8	$\frac{1.72E9(.0845)(.699)}{[.15,.17][.63,2.4][.6,26][.7,75]}\frac{1}{[.7,9]}$	8/10/8	4/4/4	2.14	0.192	22.02	138.36	
3-1	$\frac{1.17E8(.0847)(.6987)}{[.17,.16][.97,4.22][.6,26][.7,75]}$	5/3/4	3/2/2	5.60	0.059	6.80	42.74	Good
3-12	$\frac{2.35E8(.0847)(.6987)}{[.17,.16][.97,4.22][.6,26][.7,75]}\frac{1}{[.7,2]}$	7/9	4/5	1.16	0.317	36.37	228.49	
3-13	$\frac{6.07E8(.0847)(.6987)}{[.17,.16][.97,4.22][.6,26][.7,75]}\frac{1}{[.7,3]}$	10/10	4/5	1.25	0.279	31.98	200.97	Poor
5-1	$\frac{1.18E7(.0845)(.6989)}{[.16,.15][.68,1.7][.6,26][.7,75]}$	2/5	1/1	2.11	0.053	6.05	38.00	
5-9	$\frac{3.45E8(.0845)(.6989)}{[.16,.15][.68,1.7][.6,26][.7,75]}\frac{1}{[.7,6]}$	7/7	4/4	1.51	0.260	29.77	187.02	
5-10	$\frac{1.43E8(.0845)(.6989)}{[.16,.15][.68,1.7][.6,26][.7,75]}\frac{1}{[.7,4]}$	10/10	5/5	1.07	0.359	41.11	258.28	

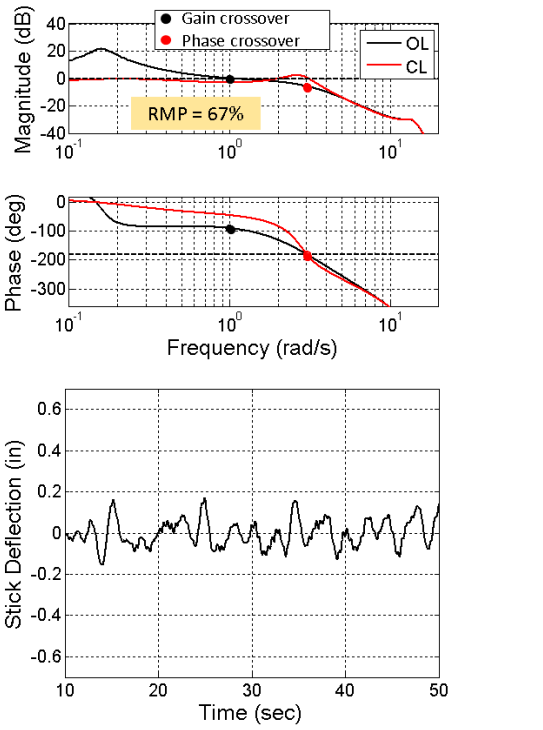

Figure 36. a) Modeled open and closed loop frequency response (poor vehicle configuration 13-13, ω_c fixed at 1 rad/s); b) Stick response.

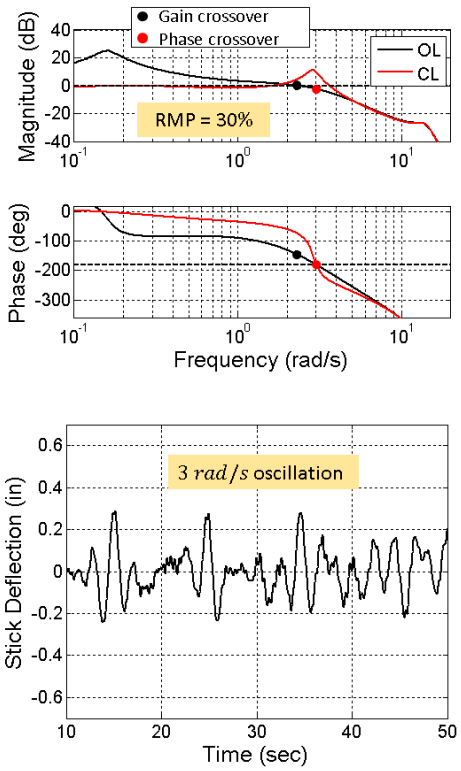

Figure 37. a) Modeled open and closed loop frequency response (poor vehicle configuration 13-13, ω_c fixed at 2.2 rad/s); b) Stick response.

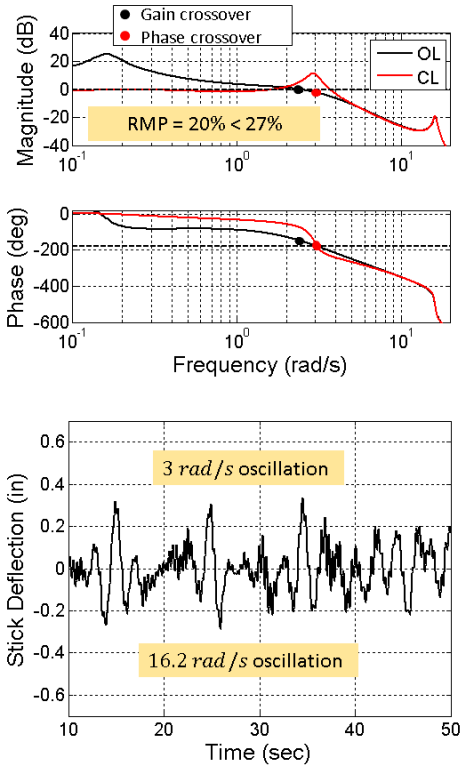

Figure 38. a) Modeled open and closed loop frequency response (poor vehicle configuration 13-13, ω_c fixed at 2.4 rad/s); b) Stick response.

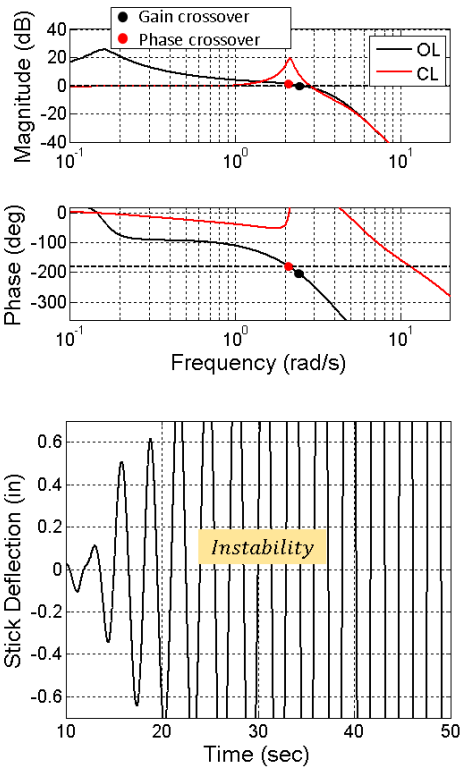

Figure 39. a) Modeled open and closed loop frequency response (poor vehicle configuration 13-13, ω_c fixed at 2.45 rad/s); b) Stick response.

Examining the good vehicle configuration (3-1), crossover is set to 2 rad/s in Figure 40 producing an

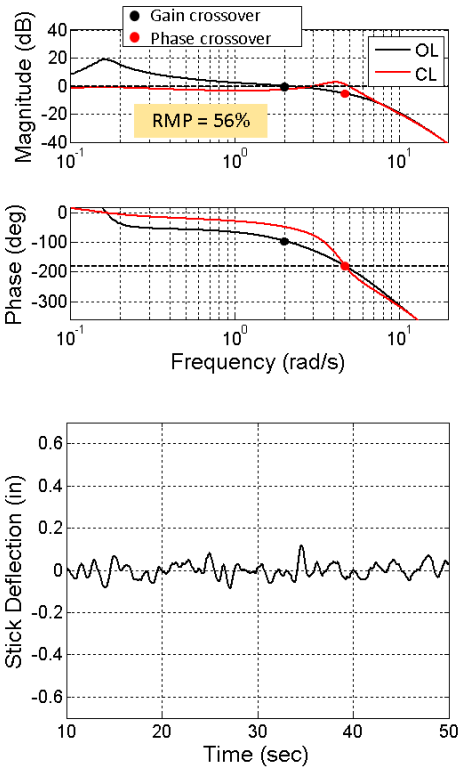

Figure 40. a) Modeled open and closed loop frequency response (good vehicle configuration 13-1, ω_c fixed at 2 rad/s); b) Stick response.

RMP of 56%. In Figure 41 crossover is increased to 5 rad/s, RMP has dropped to 32%, and a low-amplitude 18.1 rad/s ratchet is seen associated with the NM mode. Note that this mode coincides where both open and closed loop phase have crossed 360 degrees, denoted by the blue dot. In Figure 42 a crossover of 6.5 rad/s gives rise to an 8.6 rad/s oscillation associated with the rigid body mode, and the RMP at 36% is slightly above the RMP cutoff. While the high frequency 'buzz' still appears to be present it is nonetheless greatly attenuated relative to Figure 41.

The transition from a high to lower frequency oscillation when increasing crossover is a transition of dominance from the NM to the rigid body mode, and it is conceivable one could be perceived as the other. In the ratchet study conducted in Ref. 19 there were reports of ratchet and PIO for data that sometimes produced very similar frequency response. All the ratchet cases were reported by one pilot, and all the PIO cases were by two other pilots. Ref. 19 states "These differences in may be attributed to differences in pilot interpretation of ratchet and PIO." Time histories of the flight data revealed predominant stick oscillations near 8 rad/s for some runs, while others were around 12 rad/s – the former would most likely have been related to the rigid body mode, and the latter to the NM mode. There was also intermittent superposition of the two types of oscillation, which was observed in some of the APC cases just examined.

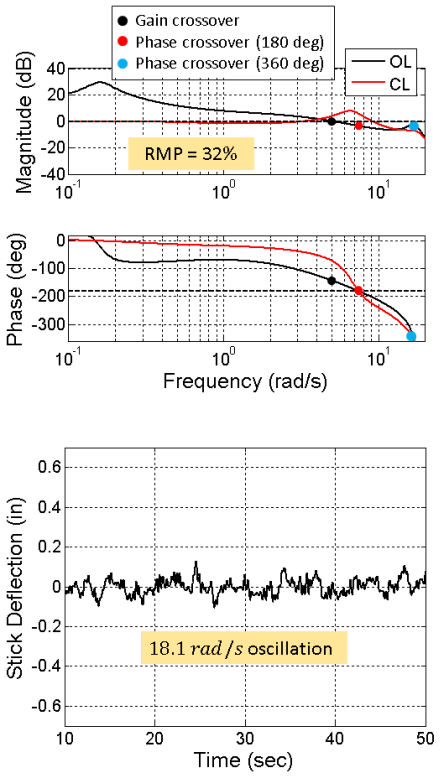

Figure 41. a) Modeled open and closed loop frequency response (good vehicle configuration 13-1, ω_c fixed at 5 rad/s); b) Stick response.

For the poor vehicle configuration, phase crossover did not change as gain crossover increased. The good configuration did see phase crossover move to higher frequency as gain crossover increased. It is intuitive that a vehicle with good ratings would offer a forgiving stability boundary in response to changes in tracking intensity, rather than a rigid boundary which would create a cliff if approached or exceeded.

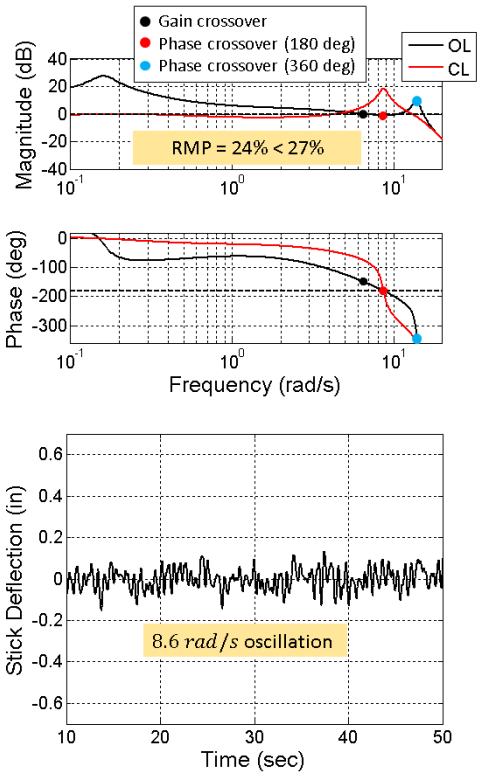

Figure 42. a) Modeled open and closed loop frequency response (good vehicle configuration 13-1, ω_c fixed at 6.5 rad/s); b) Stick response.

9. CONTROL STRATEGY AND NOISE

The lead and lag terms in the pilot's NM feedback element operate differently from the Crossover Model's lead/lag compensation. Low frequency pilot dynamics are much easier to understand in terms of the Crossover Mode's direct path lead/lag, and for this discussion the pilot's NM compensation will be converted to their Crossover Model (CM) equivalent. Figure 43 shows the frequency response corresponding to the estimated pilot parameters of an APC run (roll lag = 6 rad/s), and the frequency response in Figure 44 corresponds to a run from the of best tracking performance condition (vehicle dynamics were effectively rate command). Although the crossover frequencies of the two almost match, the APC tracking performance is significantly worse (see Figure 21). This is consistent with the much larger open loop magnitude at low frequency seen in Figure 44 (which produces superior tracking). Since the two runs have similarly high crossover frequencies and similar magnitude slopes at low frequency (roughly -20dB/dec), it would be expected that Figure 43 extends crossover

by first employing lead, and later lag. Conversely, to arrive at its crossover Figure 44 would be expected to first employ lag to steepen the magnitude's slope, followed by lead. Visual inspection of the two figures corroborates this. But why didn't the pilot during the APC run use the strategy that was adopted for the rate command system to improve tracking?

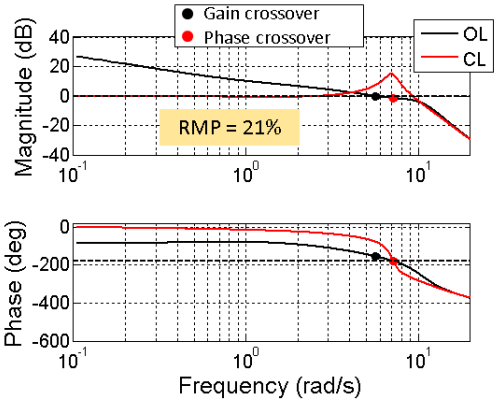

Figure 43. Estimated actual open and closed loop frequency response (APC run, roll lag = 6 rad/s).

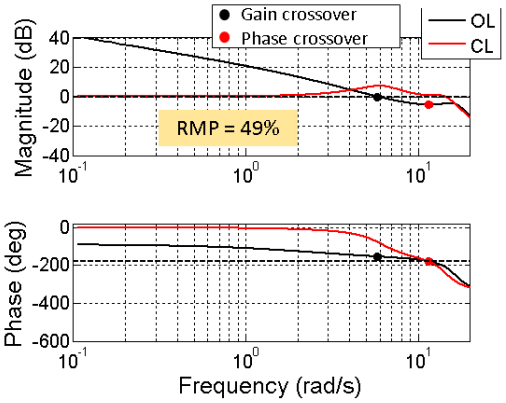

Figure 44. Estimated actual open and closed loop frequency response (best tracking performance condition run, roll lag = infinite, high stick gain, high force gradient).

Based on the high correlation observed between noise and equalization gain, the pilot model in Figure 45 shows the internal noise β_n being generated at the Visual Equalization element. Figure 46 presents the ratio of low-frequency stick noise to the linear stick response, where the ratio successively decreases starting from a roll lag of 2 rad/s until 8 rad/s. For a fixed crossover, Figure 17 shows that internal noise is roughly proportional to the equalization gain K_{EQ}. Thus, when stick noise is high (i.e., lower values of roll lag), it would make sense for the pilot to reduce K_{EQ}. For a fixed crossover, this produces low open-loop magnitude at low frequency. Conversely, when stick noise is low the pilot can afford to increase equalization, producing greater open-loop magnitude at low-frequency (i.e., better tracking) - this is behavior seen in Figure 47. Confirmation of this pilot strategy is given by the lead in Figure 48 and lag in Figure 49. When equalization is low, lead is first employed, whereas when equalization is high, lag is first employed.

APC in this experiment was the result of high stick sensitivity, high force gradient, and vehicle dynamics that enabled high crossover. APC also resulted from pilot compensation (associated with maximum performance) that pulled phase crossover into alignment with the rigid body mode ω_{RB} (the first peak of the closed loop magnitude). This contrasts with the distance separating ω_{RB} and $\omega_{c\phi}$ in Figure 44. The metric RMP is indicative of this alignment, and the relativistic aspect of RMP (separation between ω_c and $\omega_{c\phi}$ normalized by $\omega_{c\phi}$) reflects the logarithmic nature of frequency observed in numerous natural phenomena.

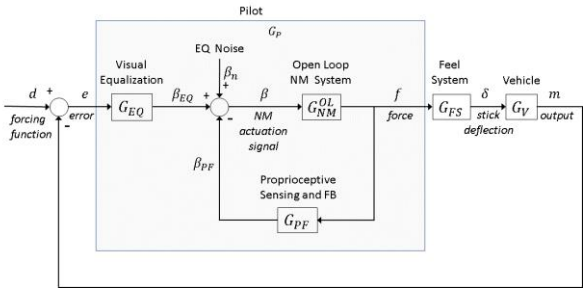

Figure 45. Revised pilot model showing internal noise generated by the Visual Equalization element.

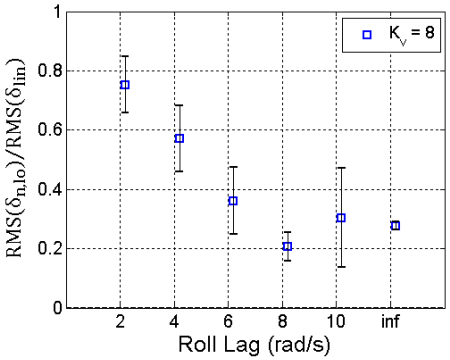

Figure 46. RMS ratio of low frequency stick noise to linear stick response versus roll lag (K_{FG} = 2.8 lb/in).

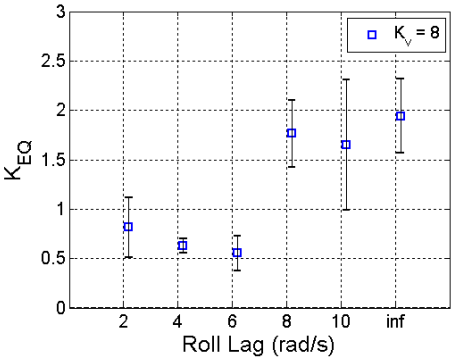

Figure 47. Pilot equalization gain versus roll lag (K_{FG} = 2.8 lb/in).

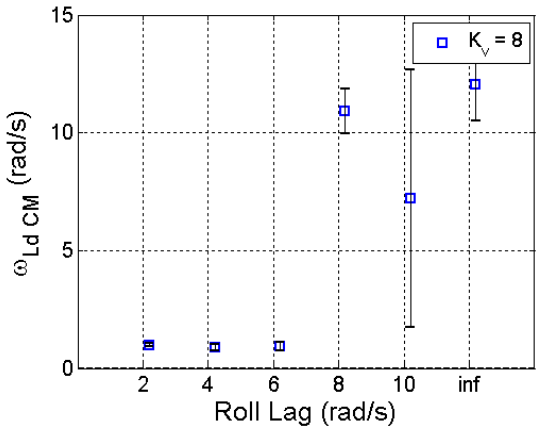

Figure 48. Pilot lead (Crossover Model equivalent) versus roll lag (K_{FG} = 2.8 lb/in).

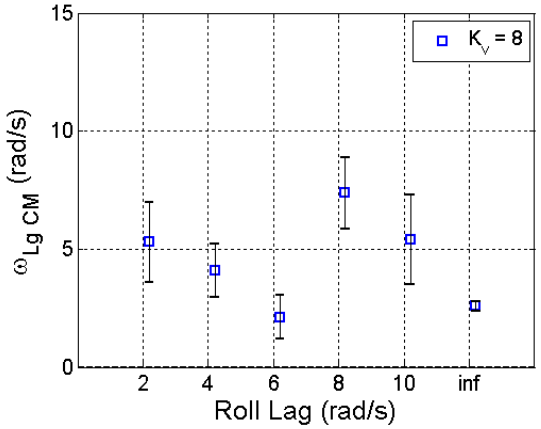

Figure 49. Pilot lag (Crossover Model equivalent) versus roll lag (K_{FG} = 2.8 lb/in).

10. CONCLUSIONS

A human-in-the-loop simulation experiment using an active sidestick where the independent variables were stick force gradient, stick sensitivity, and roll lag frequency investigated pilot model factors that contribute to Adverse Pilot Coupling (APC). A specific combination of the experimental variables was observed to significantly influence the occurrence and repeatability of APC. Departing from the traditional method of using a high-frequency sum-of-sines forcing function to identify a pilot's NM frequency response, a less intrusive approach leveraged internal noise as the NM forcing function. Preliminary results indicated that pilot internal noise originates primarily from the pilot visual equalization element and is directly proportional to the ratio of equalization gain and gain crossover frequency. The influence of equalization noise on pilot control strategy was examined.

Consistent with a previous study the experimental data showed that the peak magnitude of the open loop NM mode strongly affects high frequency roll ratchet. The current work identified that a phase crossing at 360 degrees near the vicinity of the open loop NM indicates a likelihood of roll ratchet. An adaptive pilot model was shown to produce behavior that closely matched the experimental results by incorporating: 1) tracking error and NM peak magnitude in its cost function, and 2) the observed relationship between noise and visual equalization.

Based on APC occurrence in the study, a new metric, Relative Margin Proximity (RMP), was proposed for assessing APC risk. RMP is defined as the separation between ω_c and $\omega_{c\phi}$ normalized by $\omega_{c\phi}$. A RMP threshold of approximately 27% appears to reflect propensity for APC and warrant further examination. The relativistic aspect of RMP reflects the logarithmic nature of frequency observed in numerous natural phenomena.

The pilot model was used to investigate vehicle configurations from an experimental data base that had been rated for APC severity. The RMP values produced by the pilot model for these configurations were consistent with their APC ratings. Simulation with the pilot model indicated that vehicle configurations with poor APC ratings exhibit a phase crossover and rigid body mode that does not move to higher frequency as gain crossover frequency increases (conversely rightward phase crossover movement is associated with good ratings). It was demonstrated with the adaptive pilot that transition from rigid body mode oscillation to NM mode-related oscillation is not only possible but has likely occurred based on previous test pilot ratings of ratchet and PIO events.

Higher frequency APC tends to be more of an annoyance (for short-term operation) rather than a hindrance, corroborated by the low tracking error for the APC condition observed in the experimental data. Thus, the pilot appears to accept the nuisance of ratchet since the pilot compensation that produces it also offers the best performance. This behavior was corroborated by the adaptive pilot model.

It is proposed that roll ratchet is re-classified as Category I APC (linear pilot-vehicle oscillations) since: 1) ratchet's source of power (pilot noise) appears to be linearly related to the pilot's visual equalization gain, and 2) the NM system response is essentially linear.

Relevant to today's automated cockpit, suddenly shifting operation within the cockpit from supervised automation to manual control can amplify the risk for APC due to large and variable pilot time delays. Currently there is no reliable quantitative method for definitively predicting APC or assessing it during human-in-loop operation. The Relative Margin Proximity (RMP) metric, and the adaptive pilot and internal noise model developed in this work may provide such prognostic and diagnostic capabilities. Future work will address how RMP can be computed in real time during flight.

Presented at the 48th European Rotorcraft Forum, Switzerland, 6-8th September 2022.

11. NOTATION

B	=	Bedford workload rating
d	=	Forcing function signal
CL	=	Closed loop
e	=	Error signal
f	=	Force
FS	=	Feel system
G_{xy}	=	Transfer function, x output y input
G_{NM}^{OL}	=	Pilot OL NM transfer function
K_p	=	Pilot gain
K_{FG}	=	Stick force gradient
K_V	=	Vehicle gain
n	=	Noise
NM	=	Neuromuscular
OL	=	Open loop
PF	=	Proprioceptive feedback
PSD	=	Power spectral density
s	=	Laplace transform variable
SD	=	Standard deviation
S_{xx}	=	PSD of signal x
t	=	Time
δ	=	Stick signal
σ_x^2	=	Variance (power) of signal x
ζ	=	Damping ratio
τ	=	Pilot time delay (sec)
ω	=	Angular frequency, rad/s
ω_c	=	Crossover frequency, rad/s
ω_{Ld}	=	Pilot proprioceptive lead frequency, rad/s
ω_{Lg}	=	Pilot proprioceptive lag frequency, rad/s

12. ACKNOWLEDGMENTS

This work was supported by cooperative agreement 80NSSC19M0228 between the U.S. Army DEVCOM Aviation & Missile Center and San Jose State University.

1 Klyde, David H., Duane T. McRuer, and Thomas T. Myers. Unified Pilot-Induced Oscillation Theory. Volume 1. PIO Analysis with Linear and Nonlinear Effective Vehicle Characteristics, Including Rate Limiting. Systems Technology Inc., Hawthorne CA, 1995
2 Johnston, Donald E., and Duane T. McRuer. Investigation of interactions between limb-manipulator dynamics and effective vehicle roll control characteristics. No. H-1320. NASA, 1986.
3 National Research Council 1997. Aviation Safety and Pilot Control: Understanding and Preventing Unfavorable Pilot-Vehicle Interactions. Washington, DC: The National Academies Press. https://doi.org 10.17226/5469.
4 Anon., "Handling Qualities Requirements for Military Rotorcraft, ADS-33E-PRF". U.S. Army Aviation and Missile Command, Mar, 2000.
5 Standard, Military. "Flying qualities of piloted aircraft." US Dept. of Defense MIL-STD-1797A (1990).
6 Johnston, Donald E., and Duane T. McRuer. Investigation of interactions between limb-manipulator dynamics and effective vehicle roll control characteristics. No. H-1320. NASA, 1986.
7 Magdaleno, R. P., Duane T. Mc Ruer, and George P. Moore. "Small perturbation dynamics of the neuromuscular system in tracking tasks." (1968).
8 Magdaleno, Raymond E., and Duane T. Mc Ruer. Experimental validation and analytical elaboration for models of the pilot's neuromuscular subsystem in tracking tasks. No. NASA-CR-1757. NASA, 1971.
9 Johnston, Donald E., and Bimal L. Aponso. "Design considerations of manipulator and feel system characteristics in roll tracking." (1988).
10 Hess, Ronald A. "Unified theory for aircraft handling qualities and adverse aircraft-pilot coupling." Journal of Guidance, Control, and Dynamics 20.6 (1997): 1141-1148.
11 Mulder, Max, et al. "Manual control cybernetics: State-of-the-art and current trends." IEEE Transactions on Human Machine Systems 48.5 (2017): 468-485.
12 Bachelder, Edward, and Bimal Aponso. "The Feel System is an Extension of Both the Vehicle and Neuromuscular Systems." 47th European Rotorcraft Forum, 2021.
13 Magdaleno, Raymond E., and Duane T. Mc Ruer. "Experimental validation and analytical elaboration for models of the pilot's neuromuscular subsystem in tracking tasks." (1971).
14 Gordon-Smith, M. "An Investigation into Some Aspects of the Human Operator Describing Function While Controlling a Single Degree of Freedom." NASA Special Publication 215 (1970): 203
15 McRuer, D. T. and Krendel, E. S., "Mathematical Models of Human Pilot Behavior," No. AGARDograph No. 188, November 1973.
16 Bachelder, Edward N., and Martine Godfroy-Cooper. "Pilot Workload Estimation: Synthesis of Spectral Requirements Analysis and Weber's Law." AIAA Scitech 2019 Forum. 2019.
17 Bachelder, E., Lusardi, J., and Aponso, B. "Neuromuscular Response Comparison for Center and Side Stick Positions." Vertical Flight Society 78th Annual Forum & Technology Display, Fort Worth, TX. 2021.
18 Zaychik, Larisa E., et al. "Effect of feel system characteristics on pilot model parameters." IFAC-PapersOnLine 49.32 (2016): 165-170.
19 Bailey, R. E, and L. H. Knotts, "Interactions of Feel System and Flight Control Systems Dynamics on Lateral Flying Qualities," NASA CR-179445, 1990.
20 Bachelder, E., Aponso, B. "Human Pilot Control Adaptation: A Physiological Interpretation." AIAA Scitech 2021.
21 Bachelder, Ed, and David Klyde. "Wavelet-based analysis of roll ratchet using a flight test database." AIAA Atmospheric Flight Mechanics Conference and Exhibit. 2003.
22 Bailey, R. E, and L. H. Knotts, "Interactions of Feel System and Flight Control Systems Dynamics on Lateral Flying Qualities," NASA CR-179445, 1990.
23 Mitchell, D. G., B. L. Aponso, and D. H. Klyde, Effects of Cockpit Lateral Stick Characteristics on Handling Qualities and Pilot

Dynamics, NASA CR-4443, June 1992.
24 Bachelder, E., Aponso,.B. “Novel Techniques for Characterizing and Testing Aircraft Handling Qualities.” Vertical Flight Society 2020 Rotorcraft Handling Qualities Technical Meeting. Huntsville, Alabama. 2000.
25 Magdaleno, Raymond E., and Duane T. Mc Ruer. "Experimental validation and analytical elaboration for models of the pilot's neuromuscular subsystem in tracking tasks." (1971).
26 Roscoe, A. H., and Ellis, G. A., “A subjective rating scale assessing pilot workload in flight. A decade of practical use. Royal Aerospace Establishment.” Technical Report 90019. Farnborough. UK: Royal Aerospace Establishment, 1990.
27 Bjorkman, Eileen A., Captain, USAF, Flight Test Evaluation of Techniques to Predict Longitudinal Pilot lnduced Oscillations, Thesis AFIT/GAE/AA/86J-1, Air Force Institute of Technology, Wright-Patterson Air Force Base, Ohio, Dec. 1986.

